The Astrophysical Journal Letters, 784:L40 (6pp), 2014 April 1 doi:10.1088/2041-8205/784/2/L40

NuSTAR DISCOVERY OF A CYCLOTRON LINE IN KS 1947+300

Felix Fürst[1], Katja Pottschmidt[2,3], Jörn Wilms[4], Jamie Kennea[5], Matteo Bachetti[6,7], Eric Bellm[1], Steven E. Boggs[8], Deepto Chakrabarty[9], Finn E. Christensen[10], William W. Craig[8], Charles J. Hailey[11], Fiona Harrison[1], Daniel Stern[12], John A. Tomsick[8], Dominic J. Walton[1], and William Zhang[13]
[1] Cahill Center for Astronomy and Astrophysics, California Institute of Technology, Pasadena, CA 91125, USA
[2] Center for Space Science and Technology, University of Maryland Baltimore County, Baltimore, MD 21250, USA
[3] CRESST and NASA Goddard Space Flight Center, Astrophysics Science Division, Code 661, Greenbelt, MD 20771, USA
[4] Dr. Karl-Remeis-Sternwarte and ECAP, Sternwartstr. 7, D-96049 Bamberg, Germany
[5] Department of Astronomy and Astrophysics, The Pennsylvania State University, University Park, PA 16802, USA
[6] Université de Toulouse, UPS-OMP, IRAP, F-31400 Toulouse, France
[7] CNRS, Institut de Recherche en Astrophysique et Planétologie, F-31028 Toulouse, Cedex 4, France
[8] Space Sciences Laboratory, University of California, Berkeley, CA 94720, USA
[9] Kavli Institute for Astrophysics and Space Research, Massachusetts Institute of Technology, Cambridge, MA 02139, USA
[10] DTU Space, National Space Institute, Technical University of Denmark, Elektrovej 327, DK-2800 Lyngby, Denmark
[11] Columbia Astrophysics Laboratory, Columbia University, New York, NY 10027, USA
[12] Jet Propulsion Laboratory, California Institute of Technology, Pasadena, CA 91109, USA
[13] NASA Goddard Space Flight Center, Astrophysics Science Division, Code 662, Greenbelt, MD 20771, USA
Received 2014 February 12; accepted 2014 March 5; published 2014 March 19

ABSTRACT

We present a spectral analysis of three simultaneous *Nuclear Spectroscopy Telescope Array* and *Swift*/XRT observations of the transient Be-neutron star binary KS 1947+300 taken during its outburst in 2013/2014. These broadband observations were supported by *Swift*/XRT monitoring snapshots every three days, which we use to study the evolution of the spectrum over the outburst. We find strong changes of the power-law photon index, which shows a weak trend of softening with increasing X-ray flux. The neutron star shows very strong pulsations with a period of $P \approx 18.8$ s. The 0.8–79 keV broadband spectrum can be described by a power law with an exponential cutoff and a blackbody component at low energies. During the second observation we detect a cyclotron resonant scattering feature at 12.5 keV, which is absent in the phase-averaged spectra of observations 1 and 3. Pulse phase-resolved spectroscopy reveals that the strength of the feature changes strongly with pulse phase and is most prominent during the broad minimum of the pulse profile. At the same phases the line also becomes visible in the first and third observation at the same energy. This discovery implies that KS 1947+300 has a magnetic field strength of $B \approx 1.1 \times 10^{12}(1+z)$ G, which is at the lower end of known cyclotron line sources.

Key words: accretion, accretion disks – radiation: dynamics – stars: neutron – X-rays: binaries – X-rays: individual (KS 1947+300)

Online-only material: color figures

1. INTRODUCTION

KS 1947+300 was independently discovered with *Mir-Kvant*/TTM by Borozdin et al. (1990) and with *CGRO*/BATSE by Finger et al. (1994) and Chakrabarty et al. (1995) during outbursts in 1989 and 1994, respectively. Swank & Morgan (2000) used *RXTE* data during an outburst in 2000 and the 18.7 s pulse period to identify both detections as the same accreting neutron star. The optical companion was identified by Negueruela et al. (2003) as a Be-type star at a distance of ∼10 kpc, assuming a standard luminosity. Galloway et al. (2004) determined the orbit and found an orbital period of $P_{\rm orb} = 41.5$ days, with a very low eccentricity of $e = 0.034 \pm 0.007$.

In 2000 *RXTE* performed an extensive campaign to monitor a large outburst that reached a peak flux of 120 mCrab in the 1.5–12 keV band. Galloway et al. (2004) found that the energy spectrum could be described with a simple Comptonization model (`compTT`; Titarchuk 1994; Hua & Titarchuk 1995), a model often applied to highly magnetized neutron stars. They found no source-intrinsic absorption, but a broad excess around 10 keV which they described with a hot blackbody component with $kT_{\rm bb} = 3$–4 keV.

Using *BeppoSAX* data taken during the decay of the same major outburst, Naik et al. (2006) found a similar spectral shape but a much cooler blackbody component, $kT_{\rm bb} \approx 0.6$ keV. They additionally found evidence for an FeKα line at ∼6.6 keV.

The major outburst was followed by a series of weaker outbursts, the strongest of which occurred in 2004 April and reached ∼45 mCrab in the 1.5–12 keV energy band. This series of outbursts was serendipitously monitored by *International Gamma-Ray Astrophysics Laboratory* (*INTEGRAL*) during its Galactic plane scans. Tsygankov & Lutovinov (2005) described the *INTEGRAL*/ISGRI and JEM-X spectra using a power law with a high-energy cutoff and found indications for a spectral softening with increased flux.

Accreting neutron stars sometimes show cyclotron resonant scattering features (CRSFs) in their hard X-ray spectra. These absorption-like lines are the only way to directly measure the magnetic field strength close to the neutron star surface. They are produced by photons that scatter off electrons quantized onto Landau-levels in the strong magnetic field ($B \approx 10^{12}$ G) of the neutron star. Their energy is directly related to the strength of the magnetic field in the line forming region via the "12-B-12"-rule:

$$E_{\rm CRSF} = 11.57 \times B_{12}(1+z)\,{\rm keV}, \quad (1)$$

where B_{12} is the magnetic field in 10^{12} G and z the gravitational redshift (for a detailed discussion see, e.g., Schönherr et al. 2007). Theoretically CRSF could also result in emission features (Schönherr et al. 2007), but there is only little observational evidence to date (a possible detection was reported for 4U 1626−67, see Iwakiri et al. 2012). Despite coverage with

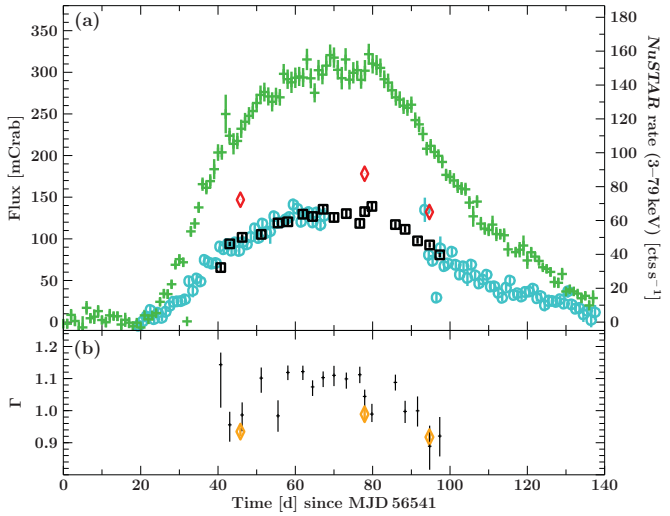

Figure 1. (a) Light curve of the 2013 outburst. Data from *Swift*/BAT (15–50 keV, Krimm et al. 2013) are shown as green crosses, MAXI (2–20 keV) as blue circles, *Swift*/XRT (0.5–8 keV) as black squares, and *NuSTAR*/FPMA (3–79 keV) as red diamonds. All data are scaled to the Crab count rate in the respective energy band. The *NuSTAR* count rate for the *NuSTAR* data is shown on the right-hand *y*-axis. (b) Best-fit power-law index Γ of the *Swift*/XRT spectra; for details of the model see the text. The orange diamonds show combined XRT and *NuSTAR* results.

(A color version of this figure is available in the online journal.)

RXTE, *BeppoSAX*, and *INTEGRAL*, a CRSF was not detected in previous outbursts of KS 1947+300 (Naik et al. 2006; Galloway et al. 2004; Tsygankov & Lutovinov 2005).

KS 1947+300 has been in quiescence from 2004–2013. In 2013 October MAXI (Matsuoka et al. 2009) detected increased flux levels (Kawagoe et al. 2013). The beginning of an outburst was immediately confirmed by *Swift*/XRT (Kennea et al. 2013) and monitored by *Swift*/Burst Alert Telescope (BAT). We triggered *Swift*/XRT ∼1 ks snapshot observations every three days to monitor the outburst in soft X-rays (Figure 1). It reached a peak flux of ∼130 mCrab in the 3–10 keV energy band, very comparable to the maximum of the bright 2000 outburst (Naik et al. 2006). Additionally, we triggered three observations with the *Nuclear Spectroscopy Telescope Array* (*NuSTAR*; Harrison et al. 2013). An overview of the observations and their exposure times can be found in Table 1.

2. OBSERVATIONS AND DATA REDUCTION

2.1. NuSTAR

NuSTAR consists of two independent grazing incidence telescopes focusing X-rays between 3–79 keV onto two focal plane modules, FPMA and FPMB. We used the standard NUSTARDAS software v1.2.0 as distributed with HEASOFT 6.14 to extract spectra and light curves. *NuSTAR* spectra were used between 3–60 keV. Above 60 keV the calibration at the time of writing shows increased systematic uncertainties, and we therefore do not use those data. A detailed analysis of the high-energy calibration will be presented in a forthcoming publication. The source data were extracted from a 130″ radius circular region centered at $\alpha_{J2000} = 19^{h}49^{m}36^{s}$ and $\delta_{J2000} = +30^{\circ}12'22''$. Background spectra were extracted from a circular region with 105″ radius as far away from the source as possible. This formally introduces systematic uncertainties in the background estimation, but since KS 1947+300 is at least a factor of 40 brighter than the background at all energies, the influence on the source flux is negligible. Light curves were extracted with a resolution of 1 s, the resolution corresponding to dead-time measurements in the standard operating mode.

Table 1
Observation log for the Three Simultaneous Observations

Observatory/ Instrument	ObsID	Start Date MJD (days)	Exposure (ks)	Pulse Period (s)
NuSTAR	80002015002	56586.79	18.4	18.80584(16)
Swift/XRT	00032990003	56587.25	0.37	
NuSTAR	80002015004	56618.91	18.6	18.78399(7)
Swift/XRT	00032990013	56618.94	0.93	
NuSTAR	80002015006	56635.75	25.4	18.77088(6)
Swift/XRT	00032990020	56635.67	0.91	

2.2. Swift/XRT

Data from the *Swift*/XRT (Burrows et al. 2005) were extracted following the standard guidelines,[14] using XSELECT to extract spectra and light curves and `xrtmkarf` to create the response files. All data were obtained in window timing mode. The source data were extracted from a circular region with a radius of 20 sky pixels (≈47″). Background spectra were extracted from the wings of the point-spread function using an annular region between 90 and 110 pixels radius (212″ and 259″, respectively). With the X-Ray Telescope (XRT), KS 1947+300 is a factor of 50 brighter than the background at all energies, rendering small uncertainties in the background negligible. We used the XRT spectra in the energy range between 0.8–10 keV. At lower energies the windowed timing mode shows larger calibration uncertainties and we therefore decided not to use those energies.[15]

2.3. Reduction Methods

All timing information for both satellites was transferred to the solar barycenter, using the FTOOL `barycorr` and the DE-200 solar system ephemeris (Standish et al. 1992), and corrected for the binary motion using the ephemeris by Galloway et al. (2004). Timing and spectral analysis was performed using the Interactive Spectral Interpretation System (ISIS v1.6.2; Houck & Denicola 2000). All uncertainties are given at the 90% level ($\Delta\chi^2 = 2.7$ for one parameter of interest), unless otherwise noted.

3. PHASE-AVERAGED SPECTROSCOPY

For spectral modeling, we use FPMA and FPMB spectra as well as the corresponding XRT data for each epoch, as detailed in Table 1. The X-ray continuum is very well described with a simple power law with an exponential cutoff (model `cutoffpl` in XSPEC) plus a blackbody. The blackbody is responsible for about 50% of the flux at 2 keV and follows the overall flux evolution of the data. It likely originates from the hot-spot of the neutron star surface. The `compTT` model used by Naik et al. (2006) and Galloway et al. (2004) results in a clearly worse fit.

Naik et al. (2006) and Galloway et al. (2004) measured an absorption column toward the source which was lower than the maximal Galactic value along that line of sight (∼9×10^{21} cm^{-2}; Kalberla et al. 2005). We therefore allow the absorption to vary in our model, but require it to be the same in all three

[14] http://www.swift.ac.uk/analysis/xrt/
[15] See http://www.swift.ac.uk/analysis/xrt/digest_cal.php#abs.

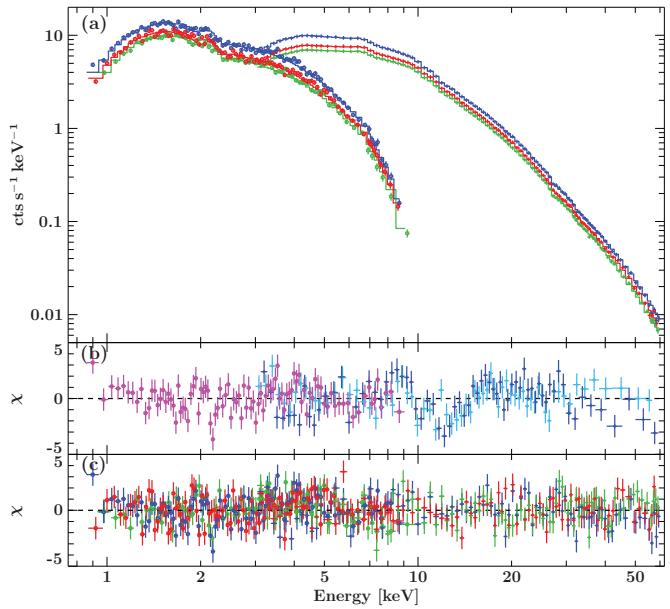

Figure 2. (a) Data and best-fit model of *Swift*/XRT (circles) and *NuSTAR*/FPMA (crosses) for all three epochs. Observation 1 is shown in red, observation 2 in blue, and observation 3 in green. (b) Residuals of observation 2 to the best-fit model without a CRSF, rebinned for plotting purposes; *Swift*/XRT is shown in magenta, *NuSTAR*/FPMA in blue and FPMB in light blue. (c) Residuals to the best-fit model including the CRSF of all three observations in terms of χ.

(A color version of this figure is available in the online journal.)

observations. We describe it using an updated version of the `tbabs` (Wilms et al. 2000) model,[16] with the corresponding abundances and cross-sections by Verner et al. (1996). Our best-fit value of $8.45 \pm 0.20 \times 10^{21}$ cm^{-2} is consistent with the 21 cm value along the line of sight and also with the $N_{\rm H}$ obtained from the reddening of the source ($A_V = 3.38$; Negueruela et al. 2003) when using the calibration of Predehl & Schmitt (1995) as updated by Nowak et al. (2012).

Adding a Gaussian FeKα line at around 6.5 keV to the continuum model we obtain a good description of the spectra, with a $\chi^2 = 3369.9$ for 3068 degrees of freedom (dof) ($\chi^2_{\rm red} = 1.10$). The data are shown in Figure 2(a). However, close inspection of the residuals of the second observation reveals significant residuals around 13 keV (see Figure 2(b)). We therefore add a multiplicative absorption line with a Gaussian optical depth profile (model `gabs` in XSPEC) to the model for the second observation. This additional component improves the fit significantly to $\chi^2 = 3284.6$ for 3063 dof ($\chi^2_{\rm red} = 1.07$, F-test false positive probability 1.5×10^{-15}, after Bevington & Robinson 1992). This model is shown in Figure 2(a), the best-fit residuals in Figure 2(c), and its parameters are given in Table 2. The fluxes are given in *NuSTAR*/FPMA normalization and we allow for small cross-calibration differences to *Swift*/XRT and FPMB using the multiplicative factors $C_{\rm XRT}$ and $C_{\rm FPMB}$, respectively.

We search for similar absorption lines in the spectra of the other two observations. For that we require the energy and width of the `gabs` component to be the same in all observations and allow only the depth to vary in a simultaneous fit to all three data sets. In both other data sets the line is not significantly detected (Table 2). The 90% uncertainties are clearly below the depth of the line during observation 2, indicating a physical change in the source spectrum over the outburst.

[16] http://pulsar.sternwarte.uni-erlangen.de/wilms/research/tbabs/

Table 2
Fit Parameters for the Best-fit Phase-averaged Model

Parameter	Obs. I	Obs. II	Obs. III
$N_{\rm H}$[a,b]	$0.848^{+0.024}_{-0.020}$	$0.848^{+0.024}_{-0.020}$	$0.848^{+0.024}_{-0.020}$
$\mathcal{F}_{1-60\,\rm keV}$[c]	7.202 ± 0.027	9.08 ± 0.04	6.491 ± 0.021
$L_{1-60\,\rm keV}$[d]	8.62 ± 0.03	10.87 ± 0.05	7.768 ± 0.024
Γ	0.928 ± 0.014	$0.982^{+0.022}_{-0.015}$	$0.927^{+0.014}_{-0.012}$
$E_{\rm cut}$ (keV)	$22.5^{+0.5}_{-0.4}$	$24.2^{+0.6}_{-0.5}$	$22.13^{+0.45}_{-0.24}$
$E_{\rm CRSF}$ (keV)[b]	$12.2^{+0.5}_{-0.7}$	$12.2^{+0.5}_{-0.7}$	$12.2^{+0.5}_{-0.7}$
$\sigma_{\rm CRSF}$ (keV)[b]	$2.5^{+1.3}_{-0.6}$	$2.5^{+1.3}_{-0.6}$	$2.5^{+1.3}_{-0.6}$
$d_{\rm CSRF}$ (keV)	$0.00^{+0.04}_{-0.05}$	$0.16^{+0.15}_{-0.05}$	$-0.05^{+0.04}_{-0.10}$
$A_{\rm BB}$[e]	$4.12^{+0.21}_{-0.20}$	$5.73^{+0.28}_{-0.52}$	$3.45^{+0.19}_{-0.18}$
kT (keV)	$0.663^{+0.017}_{-0.018}$	$0.745^{+0.017}_{-0.026}$	$0.636^{+0.023}_{-0.016}$
A(Fe Kα)[f]	$1.78^{+0.20}_{-0.19}$	$2.28^{+0.22}_{-0.25}$	$1.20^{+0.16}_{-0.12}$
E(Fe Kα)(keV)[g]	$6.575^{+0.030}_{-0.032}$	$6.563^{+0.031}_{-0.028}$	$6.539^{+0.029}_{-0.031}$
σ(Fe Kα)(keV)[g]	0.29 ± 0.05	0.31 ± 0.04	0.25 ± 0.04
$C_{\rm XRT}$	0.967 ± 0.014	$0.966^{+0.012}_{-0.015}$	$0.982^{+0.017}_{-0.015}$
$C_{\rm FPMB}$	1.0207 ± 0.0023	1.0308 ± 0.0021	1.0232 ± 0.0021

Notes.
[a] In 10^{22} cm^{-2}.
[b] Parameter tied across observations.
[c] Unabsorbed flux in 10^{-9} erg s^{-1} cm^{-2}.
[d] Luminosity for a distance of 10 kpc in 10^{37} erg s^{-1}.
[e] In 10^{36} erg s^{-1} for a distance of 10 kpc.
[f] In 10^{-3} ph s^{-1} cm^{-2}.
[g] In keV.

3.1. Time-resolved Spectral Analysis

To study the evolution of the spectrum over the outburst we use all available *Swift*/XRT data between MJD 56581–56639, and describe them with the same `cutoffpl` plus `bbody` model as the time-averaged spectra. We fix the cutoff energy at 23.2 keV, the average value in the *NuSTAR* data, and the absorption column to 8.45×10^{21} cm^{-2}, since the Galactic absorption column should not vary.

We find a strong degeneracy between the power-law slope and the blackbody temperature due to the limited energy range covered by *Swift*/XRT. From the simultaneous *NuSTAR* and *Swift*/XRT spectra it becomes clear, however, that an almost linear correlation between the blackbody temperature and the unabsorbed 3–10 keV flux is present,

$$kT_{\rm bb} = m \times \mathcal{F}_{3-10\,\rm keV}, \quad (2)$$

where $kT_{\rm bb}$ is measured in keV and $\mathcal{F}_{3-10\,\rm keV}$ in keV s^{-1} cm^{-2}. In the simultaneous fits we find $m = 0.576 \pm 0.010$ s cm^2. We use this correlation to tie the blackbody temperature to the X-ray flux in the time-resolved XRT spectra and consequently replace the degeneracy with an empirically motivated correlation.

The remaining free parameters in the model are the photon index of the power law, the 3–10 keV flux, and the relative normalization of the blackbody component. The latter does not show significant changes with time. The model describes all 19 XRT spectra relatively well, with an average $\chi^2_{\rm red} = 1.05$ for 429 dof.

As shown in Figure 1(b), the photon index is highly variable and seems to soften with increased X-ray flux. This correlation is marginally significant at a bit above the 1σ level, with Spearman's rank correlation coefficient $\rho = 0.31$. It also becomes clear that all three *NuSTAR* observations were performed during phases with relatively hard spectra. Tsygankov &

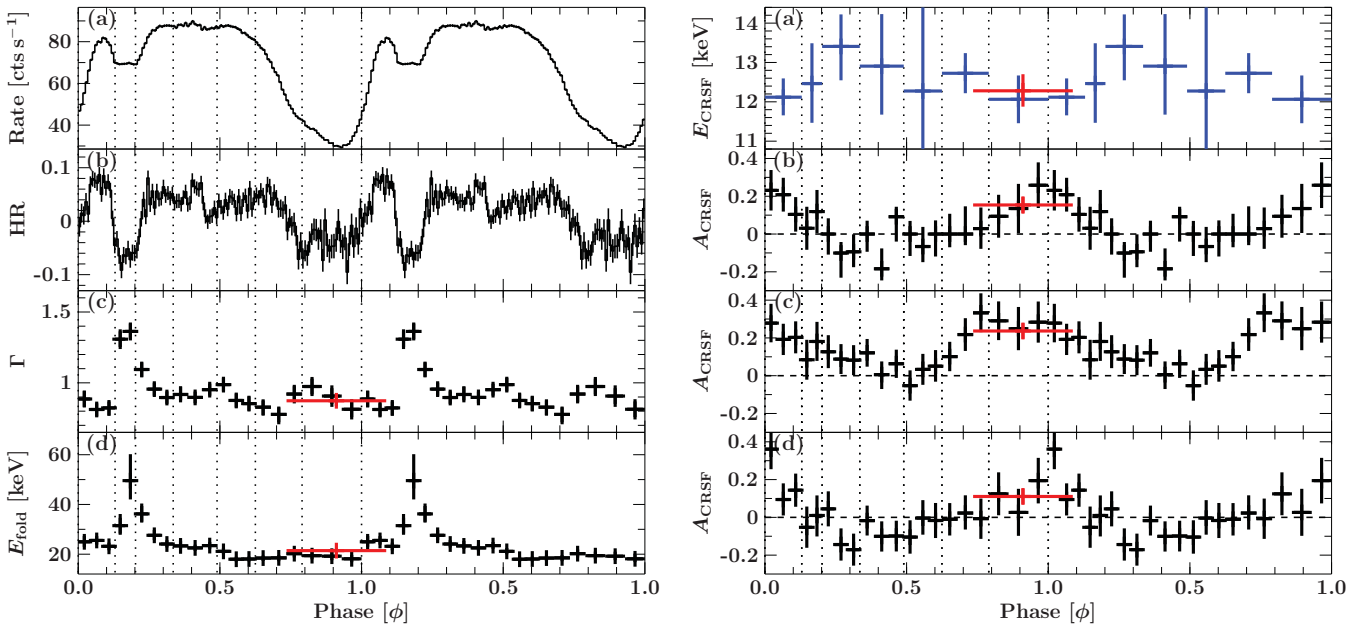

Figure 3. Results of the phase-resolved spectroscopy. The left panel shows for observation 2 the (a) pulse profile between 3–79 keV, (b) hardness ratio $(H-S)/(H+S)$ between the energy bands $S = 4.5$–6 keV and $H = 10$–15 keV. The dotted lines indicate the seven, wider phase bins used to measure the CRSF energy. The photon index Γ and the folding energy are shown in panels (c) and (d), respectively. The right panel shows the parameters of the CRSF: (a) line energy for the second observation, ((b)–(d)) line strength for the first, second, and third observation, respectively. The red data points show the results of the phase bin covering the phases with the most significant CRSF in observation 2; see the text for details. The pulse is repeated once for clarity.

(A color version of this figure is available in the online journal.)

Lutovinov (2005) found a similar correlation between then photon index and the X-ray luminosity in the harder *RXTE* energy band (3–100 keV).

4. PHASE-RESOLVED SPECTROSCOPY

To investigate changes with viewing angle onto the neutron star we split each *NuSTAR* data set into 20 phase bins. For this analysis we did not use the *Swift*/XRT data, as their short exposure does not allow us to split them up further. We define the phase bins to stretch over intervals of similar flux and hardness ratio; see Figure 3. The pulse profile changes drastically with energy, developing from one broad pulse to a double-peaked profile, with a narrow primary and broader secondary peak above ∼25 keV (see also Naik et al. 2006).

To define the phase bins individually for each observation, we first measure the local pulse period by folding the cleaned *NuSTAR* event list on trial periods around the expected period of 18.8 s, following the description given by Leahy & Scott (1998). The uncertainties are estimated by phase-connecting pulse profiles from the beginning and end of each observation. We do not allow for a change in the pulse period during one observation, but the error introduced is below the precision needed for the analysis presented here. The measured periods show a continuous spin-up over the duration of the outburst (see Table 1), in agreement with the *Swift*/XRT snapshots and the *Fermi*/Gamma-ray Burst Monitor pulsar monitoring[17] (Finger et al. 2009).

To describe the phase-resolved spectra we use the same model as for the phase-averaged spectrum, but fix the line energies and widths of the CRSF and the FeKα line as well as the temperature of the blackbody due to the reduced statistical quality of the spectra. This model results in a very good description of the data in all phase bins, with an average $\chi^2_{\rm red} = 1.02$ for 345 dof.

Figure 3 shows the continuum parameters only for the second observation, since it provides the best statistics, but the other two observations show very similar behavior. Both the photon index Γ and the folding energy $E_{\rm fold}$ show a very strong dependence on phase, confirming the results by Naik et al. (2006) at a much higher resolution in phase space (Figure 3 left, panels (c) and (d)). Between phase 0.1–0.2 we observe a strong increase in Γ and $E_{\rm fold}$, coincident with the small dip between the narrow first peak and the broad main peak.

The strength of the CRSF shows a very interesting behavior with pulse phase, as shown for all observations in Figure 3, right panel. As expected from the phase-averaged spectra, the line is clearly strongest in observation 2, being detectable over a wide phase range between phases 0.6–1.3. During the main peak of the pulse profile the line strength drops to 0. In observation 1 the line is also significantly detected in absorption between phases 0.9–1.1. Around phase 0.3 there are low significance indications that the line is instead visible in emission. In observation 3 the line strength is scattering around 0, only one phase bin around phase 1.0 shows an absorption line clearly above the 95% limit.

In the phase-resolved spectra we allow the iron line normalization and the blackbody normalization to vary to obtain a statistically acceptable fit (not shown in Figure 3). We carefully checked that any variation in these parameters does not influence the strength of the CRSF. While the iron line shows the largest equivalent width during the minimum of the pulse profile, i.e., at the same phases where the CRSF is most prominent, it does not influence the spectral shape at the CRSF energy. The blackbody did not vary significantly over the pulse phase.

To investigate the energy dependence of the CRSF with pulse phase, we extracted spectra from observation 2 using seven wider phase bins to increase the signal-to-noise ratio. For these spectra we also allow the iron line energy and width, as well

[17] http://gammaray.nsstc.nasa.gov/gbm/science/pulsars/lightcurves/ks1947.html

as the blackbody temperature to vary. We keep the width of the CRSF fixed to the best phase-averaged value, as it otherwise became unconstrained during the fits. As can be seen in Figure 3, right panel (a), we do not detect a significant variation of the line energy with pulse phase. Between phases 0.4–0.6 we again detected no significant line, resulting in an unconstrained energy.

Besides changes with pulse phase, changes of the line energy with luminosity are quite common (see, e.g., Caballero et al. 2007; Tsygankov et al. 2010; Fürst et al. 2014, among others). To search for such a luminosity dependence between observations, we extract spectra for each observation of those phases, in which the line was significantly detected in observation 2. This approach allows us to obtain the most significant line and therefore most precise energy measurement, as indicated by the blue data points in Figure 3. We describe the spectra with the same model as for the seven wide phase bins described above. We do not detect a significant change of the line energy, with the measured values being 12.5 ± 0.7 keV, 12.3 ± 0.5 keV, and 12.2 ± 0.9 keV for observation 1, 2, and 3, respectively.

5. SUMMARY AND DISCUSSION

We have presented a spectral analysis of three *NuSTAR* observations of the Be-X-ray binary KS 1947+300 with simultaneous *Swift*/XRT data, taken during its large 2013/2014 outburst. The broad spectral coverage provided by the combination of these two instruments allowed us to discover a CRSF absorption feature around 12.5 keV. The feature was significantly detected in the phase-averaged spectrum of the brightest observation, and during the broad pulse minimum in phase-resolved spectroscopy in all observations. During the pulse maximum the feature is not seen significantly, either in absorption or emission.

The line energy and width is similar to the lines detected in 4U 0115+63 and *Swift* J1626.6−5156 (White et al. 1983; DeCesar et al. 2013). We deduce a surface magnetic field of $\sim 1.1 \times 10^{12}(1+z)$ G, assuming that the line is the fundamental line. Here z is the gravitational redshift, defined by

$$(1+z)^{-1} = \sqrt{1 - \frac{2GM}{Rc^2}}. \quad (3)$$

For typical neutron star parameters, $z \approx 0.3$ if the line-forming region is close to the surface. This magnetic field strength puts KS 1947+300 at the lower end of known cyclotron lines sources (cf. Caballero et al. 2007).

During the broad minimum phase of the pulse profile, we detect the CRSF in all three observations. The luminosity near 10^{38} erg s^{-1} puts KS 1947+300 clearly in the supercritical accretion regime, where the radiation pressure is strong enough to decelerate the in-falling matter before the neutron star surface via a radiation-dominated shock (Becker et al. 2012). In this regime, a negative correlation between the CRSF energy and luminosity is expected (Becker et al. 2012), as observed, for example, in V 0332+53 (Tsygankov et al. 2010). If the correlation were of a similar strength as observed in V 0332+53 we would not have detected it due to the very small range of luminosities sampled.

The time-resolved *Swift*/XRT spectra show a strongly variable photon index Γ over the outburst, with changes of 10% or more within three days and softening with increasing X-ray flux. This softening agrees with the expected behavior in the supercritical accretion regime, as shown by Klochkov et al. (2011) for various other sources. However, because we restricted the model to describe basically all changes in spectral hardness in the photon index, it is probable that the true physical changes are more complex than a variable photon index, e.g., the blackbody temperature might vary independently of the X-ray flux. Nonetheless, intrinsic source variability must be present.

We clearly detect a FeKα line in all data sets, with an energy significantly above the line energy for neutral iron (see Table 2) and broadened in excess of the energy resolution of *NuSTAR*. While Doppler-broadening could be responsible for part of the observed width, the increased energy indicates that the fluorescence region is slightly ionized and the observed broadening originates from a blend of FeKα at different low ionization states. The data do not allow us to disentangle different lines from one single broad line.

We would like to thank Matthias Kühnel, Ralf Ballhausen, Fritz Schwarm, and Peter Kretschmar for useful discussions. This work was supported under NASA contract No. NNG08FD60C, and made use of data from the *NuSTAR* mission, a project led by the California Institute of Technology, managed by the Jet Propulsion Laboratory, and funded by the National Aeronautics and Space Administration. We thank the *NuSTAR* Operations, Software, and Calibration teams for support with the execution and analysis of these observations. This research has made use of the *NuSTAR* Data Analysis Software (NuSTARDAS) jointly developed by the ASI Science Data Center (ASDC, Italy) and the California Institute of Technology (USA). This research has made use of ISIS functions provided by ECAP/Remeis observatory and MIT (http://www.sternwarte.uni-erlangen.de/isis/). We thank the Deutsches Zentrum für Luft- und Raumfahrt for partial support under DLR grant 50 OR 1113. We thank the anonymous referee for useful comments.

Facilities: NuSTAR, *Swift*

REFERENCES

Becker, P. A., Klochkov, D., Schönherr, G., et al. 2012, A&A, 544, A123
Bevington, P. R., & Robinson, D. K. 1992, Data Reduction and Error Analysis for the Physical Sciences (2nd ed.; New York: McGraw-Hill)
Borozdin, K., Gilfanov, M., Sunyaev, R., et al. 1990, SvAL, 16, 345
Burrows, D. N., Hill, J. E., Nousek, J. A., et al. 2005, SSRv, 120, 165
Caballero, I., Kretschmar, P., Santangelo, A., et al. 2007, A&A, 465, L21
Chakrabarty, D., Koh, T., Bildsten, L., et al. 1995, ApJ, 446, 826
DeCesar, M. E., Boyd, P. T., Pottschmidt, K., et al. 2013, ApJ, 762, 61
Finger, M. H., Beklen, E., Narayana Bhat, P., et al. 2009, in Proc. 2009 Fermi Symposium, ed. D. J. Thompson (SLAC eConf Proceedings), in press (arXiv:0912.3847)
Finger, M. H., Stollberg, M., Pendleton, G. N., et al. 1994, IAUC, 5977, 1
Fürst, F., Pottschmidt, K., Wilms, J., et al. 2014, ApJ, 780, 133
Galloway, D. K., Morgan, E. H., & Levine, A. M. 2004, ApJ, 613, 1164
Harrison, F. A., Craig, W. W., Christensen, F. E., et al. 2013, ApJ, 770, 103
Houck, J. C., & Denicola, L. A. 2000, in ASP Conf. Ser. 216, Astronomical Data Analysis Software and Systems IX, ed. N. Manset, C. Veillet, & D. Crabtree (San Francisco, CA: ASP), 591
Hua, X., & Titarchuk, L. 1995, ApJ, 449, 188
Iwakiri, W. B., Terada, Y., Mihara, T., et al. 2012, ApJ, 751, 35
Kalberla, P. M. W., Burton, W. B., Hartmann, D., et al. 2005, A&A, 440, 775
Kawagoe, A., Mihara, T., Negoro, H., et al. 2013, ATel, 5438
Kennea, J. A., Evans, P. A., Krimm, H. A., et al. 2013, ATel, 5441
Klochkov, D., Staubert, R., Santangelo, A., Rothschild, R. E., & Ferrigno, C. 2011, A&A, 532, A126
Krimm, H. A., Holland, S. T., Corbet, R. H. D., et al. 2013, ApJS, 209, 14
Leahy, D. A., & Scott, D. M. 1998, ApJL, 503, L63
Matsuoka, M., Kawasaki, K., Ueno, S., et al. 2009, PASJ, 61, 999
Naik, S., Callanan, P. J., Paul, B., & Dotani, T. 2006, ApJ, 647, 1293
Negueruela, I., Israel, G. L., Marco, A., Norton, A. J., & Speziali, R. 2003, A&A, 397, 739
Nowak, M. A., Neilsen, J., Markoff, S. B., et al. 2012, ApJ, 759, 95
Predehl, P., & Schmitt, J. H. M. M. 1995, A&A, 293, 889

Schönherr, G., Wilms, J., Kretschmar, P., et al. 2007, A&A, 472, 353
Standish, E. M., Newhall, X. X., Williams, J. G., & Yeomans, D. K. 1992, in Explanatory Supplement to the Astronomical Almanac, ed. P. K. Seidelmann (Mill Valley, CA: University Science Books), 279
Swank, J., & Morgan, E. 2000, IAUC, 7531, 4
Titarchuk, L. 1994, ApJ, 434, 570
Tsygankov, S. S., & Lutovinov, A. A. 2005, AstL, 31, 88
Tsygankov, S. S., Lutovinov, A. A., & Serber, A. V. 2010, MNRAS, 401, 1628
Verner, D. A., Ferland, G. J., Korista, K. T., & Yakovlev, D. G. 1996, ApJ, 465, 487
White, N. E., Swank, J. H., & Holt, S. S. 1983, ApJ, 270, 711
Wilms, J., Allen, A., & McCray, R. 2000, ApJ, 542, 914